

Impact of nearshore wind stress curl on coastal circulation and primary productivity in the Peru upwelling system

A. Albert,¹ V. Echevin,¹ M. Lévy,¹ and O. Aumont²

Received 3 August 2010; revised 21 September 2010; accepted 29 September 2010; published 16 December 2010.

[1] Coastal upwelling dynamics are strongly affected by alongshore wind stress and nearshore wind stress curl. A coupled physical-biogeochemical regional model and lagrangian diagnostics are used in the Peru current system to determine how the upwelling of nutrients and the primary productivity are impacted by the spatial structure of the nearshore wind stress. Three wind stress products derived from the ERS and QuikSCAT scatterometers and a smoothed QuikSCAT field, mainly differing in nearshore wind stress curl patterns, were used. Simulations are found to produce significantly different mean surface chlorophyll distributions and show that strong upwelling-favorable nearshore wind stress curl may locally induce a wide coastal productive zone through upwelling of nutrient-replete waters brought by a shoaling coastal undercurrent. Using wind stress products with realistic nearshore patterns is therefore crucial for the modeling of coupled physical-biogeochemical coastal processes.

Citation: Albert, A., V. Echevin, M. Lévy, and O. Aumont (2010), Impact of nearshore wind stress curl on coastal circulation and primary productivity in the Peru upwelling system, *J. Geophys. Res.*, 115, C12033, doi:10.1029/2010JC006569.

1. Introduction

[2] The Peruvian coast features one of the four major upwelling systems in the world ocean and shows high biological activity due to yearlong coastal upwelling induced by the trade winds. Upwelling occurs near the coast when the wind stress has an equatorward alongshore component or in the case of nearshore negative (in the Southern Hemisphere) wind stress curl. Coastal divergence of the seaward Ekman current is forced by the alongshore equatorward wind stress, whereas upward Ekman pumping results from the wind stress curl. In the Peru current system, as in other eastern boundary upwelling systems (hereafter EBUS), both coastal divergence and Ekman pumping may modulate the upwelling intensity.

[3] Surface wind products derived from spaceborne scatterometers (e.g., QuikSCAT and ERS) provide useful measurements that aid in the assessment of the two Ekman-related processes. Climatologies of scatterometer winds, which differ in spatial resolution, have widely been used in recent modeling studies of the Benguela [Blanke *et al.*, 2002, 2005], Humboldt [Penven *et al.*, 2005; Echevin *et al.*, 2008; Colas *et al.*, 2008] and California [Capet *et al.*, 2004] EBUS.

[4] One of the main limitations of these wind products is that measurements cannot be obtained near the coast. They

are limited to a distance of 25 km and 50 km from the land for QuikSCAT and ERS, respectively. Intense cross-shore wind gradients exist in this area known as the dropoff zone due to the land-sea change in surface drag, coastal orography [Edwards *et al.*, 2001] and sea surface temperature fronts [Jin *et al.*, 2009]. These gradients have a strong influence on the coastal circulation and upwelling intensity [Capet *et al.*, 2004; Renault *et al.*, 2009; Jin *et al.*, 2009] but are only marginally captured by QuikSCAT and ERS [Croquette *et al.*, 2007]. Typically, these global wind products tend to overestimate the alongshore coastal winds and to underestimate the wind stress curl, generating an excessively strong upwelling at the coast and a overly weak upwelling in the coastal band. These two caveats may compensate each other in terms of upward mass transport, however they are likely to have a strong impact on the nearshore distribution of nutrients and biological productivity. The aim of this work is to determine whether the two mechanisms compensate each other or whether one of them dominates, in the particular case of the Northern Humboldt EBUS.

[5] In this study we investigate the influence of the wind stress forcing on the coastal circulation and surface productivity in the Peru upwelling system (4°N–20°S) using a regional circulation model. We first evaluate the model realism in terms of simulated currents and biogeochemical fields. We then compare the results of the model driven by wind forcings which mainly differ in their coastal wind stress curl patterns. Results in terms of primary production and related nutrient availability are described and quantified, and the relationship between biological activity and wind forcing is thoroughly investigated.

[6] In the following sections, the model characteristics, the data and methods used are described (section 2), the

¹Laboratoire d'Océanographie et du Climat: Expérimentation et Analyses Numériques, CNRS/IRD/UPM/MNHN, Paris, France.

²Laboratoire de Physique des Océans, CNRS/IFREMER/UBO, Brest, France.

results of the simulations are presented (section 3) and we conclude with a discussion of our results (section 4).

2. Data and Tools

2.1. Scatterometer Wind Data

[7] QuikSCAT winds from the Seawind scatterometer have a 25 km spatial resolution and a 1800 km wide swath. QuikSCAT daily samples about 90% of the global oceans and operates since June 1999. In contrast, ERS 1–2 scatterometer measurements have coarser spatial and temporal resolutions, 50 km and 3 day global coverage, a 500 km wide swath and has operated between July 1991 and March 2001. The wind stress products used in this study are gridded from swath data by CERSAT (www.ifremer.fr/cersat/) on 0.5° (QuikSCAT) and 1° (ERS) resolution grids, with daily and weekly temporal resolutions, respectively. Monthly mean climatologies computed over different time periods of comparable length were constructed: 2000–2006 for QuikSCAT and 1992–2000 for ERS.

2.2. Numerical Model and Configuration

[8] Wind stress forcings are used to drive a regional coupled dynamical-biogeochemical model (ROMS/PISCES). The ROMS (Regional Ocean Modeling System) [Shchepetkin and McWilliams, 2005] dynamical model solves the primitive equations, based on the Boussinesq approximation and the hydrostatic vertical momentum balance. It is a split-explicit, free-surface oceanic model and discretized in terrain-following curvilinear coordinates. The PISCES model (Pelagic Interaction Scheme for Carbon and Ecosystem Studies) [Aumont et al., 2003] is a biogeochemical model which simulates the marine biological productivity and biogeochemical, carbon and main nutrients cycling (nitrate, phosphate, silicate and iron).

[9] The model configuration used here is similar to that described by Echevin et al. [2008]. The model domain is a rectangular grid extending from 20°S to 3°N in latitude and from 90°W to 70°W in longitude, with a $1/6^\circ$ horizontal resolution. The heat fluxes originate from the COADS climatology and include a relaxation to the COADS climatological SST [DaSilva et al., 1994]. The northern, western and southern open boundaries of the model are forced by the dynamics and biogeochemistry obtained from a monthly climatology of the ORCA 2° OGCM simulation over 1992–2000 (L. Bopp, personal communication, 2009). The surface forcing for PISCES includes atmospheric iron dust input following Tegen and Fung [1995]. For further details on the coupled model the reader is referred to the work by Aumont and Bopp [2006] and Echevin et al. [2008].

[10] In each of our experiments, ROMS/PISCES was span up for a period of 10 years and reached a statistical quasi-equilibrium for both dynamical and biogeochemical variables. The next 10 years of simulation were used to construct a climatological mean state analyzed in section 3. Three simulations were analyzed and compared: QSIM (ESIM) designates the simulation forced by QuikSCAT (ERS) wind stress fields. The third simulation named QncSIM (for QuikSCAT “no curl”) is forced by a modified version of QuikSCAT forcing in which the coastal wind dropoff has been artificially smoothed, and which is quite similar to ERS forcing in the nearshore zone.

2.3. Data Sets

[11] To assess the accuracy of our simulations, observations of several variables are used. The advanced very high resolution radiometer (AVHRR) Pathfinder satellite SST daily data at 4 km resolution are used to construct a climatology over the 1992–2006 period [Kilpatrick et al., 2001] to validate the model SST.

[12] A climatology of near-surface (~ 15 m depth) currents at 1° resolution derived from satellite-tracked surface drifting buoy available from the Global Drifter Program [Lumpkin and Garraffo, 2005] is used to evaluate near-surface model velocities.

[13] Surface chlorophyll concentrations are provided by the SeaWiFS satellite data over the 2000–2006 period [Behrenfeld and Falkowski, 1997]. Data were rebinned from the original $0.0879^\circ \times 0.0879^\circ$ grid onto the $1/6^\circ$ model grid thus reducing spatial noise and cloudiness.

[14] An in situ data set consisting of surface chlorophyll, nitrate, phosphate and silicate concentrations collected by Instituto del Mar del Peru (IMARPE) during 1992–2004 was also used. A 0.5° gridded climatological product was constructed by binning and filtering the data. A complete description of the data processing and quality control can be found in the work by Echevin et al. [2008]. A few dissolved iron measurements are also available from cross-shore transects (8°S and 13°S) off Peru during austral winter in 2000 [Bruland et al., 2005].

2.4. Lagrangian Tool

[15] The ROMS offline tracking algorithm is used to calculate numerical Lagrangian trajectories from model velocity fields [Capet et al., 2004; Carr et al., 2008]. Our experiments consist in releasing a large number of floats exactly where waters parcels are upwelled into the surface layer (between 50 and 60 m depth), and integrating the trajectories of the floats backward in time during 1 month. During the course of each upwelled water parcel’s journey from the upwelling area back to its original location 1 month before, the position, depth and nutrient content of each particule are stored every 5 days. This census is repeated every 5 days of the model climatological seasonal cycle.

3. Results

3.1. Evaluation of Model Outputs

[16] We first analyze the results of the QSIM simulation and compare the simulated variables of interest for the upwelling system with the available observations.

3.1.1. Wind Forcing

[17] The monthly mean climatology of QuikSCAT winds is interpolated onto the model grid. We show the maps of the resulting wind stress and wind stress curl in Figure 1. The model domain encompasses the eastern part of the South Pacific subtropical anticyclonic gyre. Easterly trade winds are parallel to the coast and equatorward (Figure 1a), therefore upwelling favorable along the Peruvian coasts. The wind stress intensity is stronger in the center of the subtropical gyre (16°S – 88°W) and decreases when approaching the coast. Wind stress curl is therefore positive within the gyre and negative elsewhere with values over $-1.10^{-7} \text{ N m}^{-3}$ (Figure 1b). Close to the shore, a coastal band

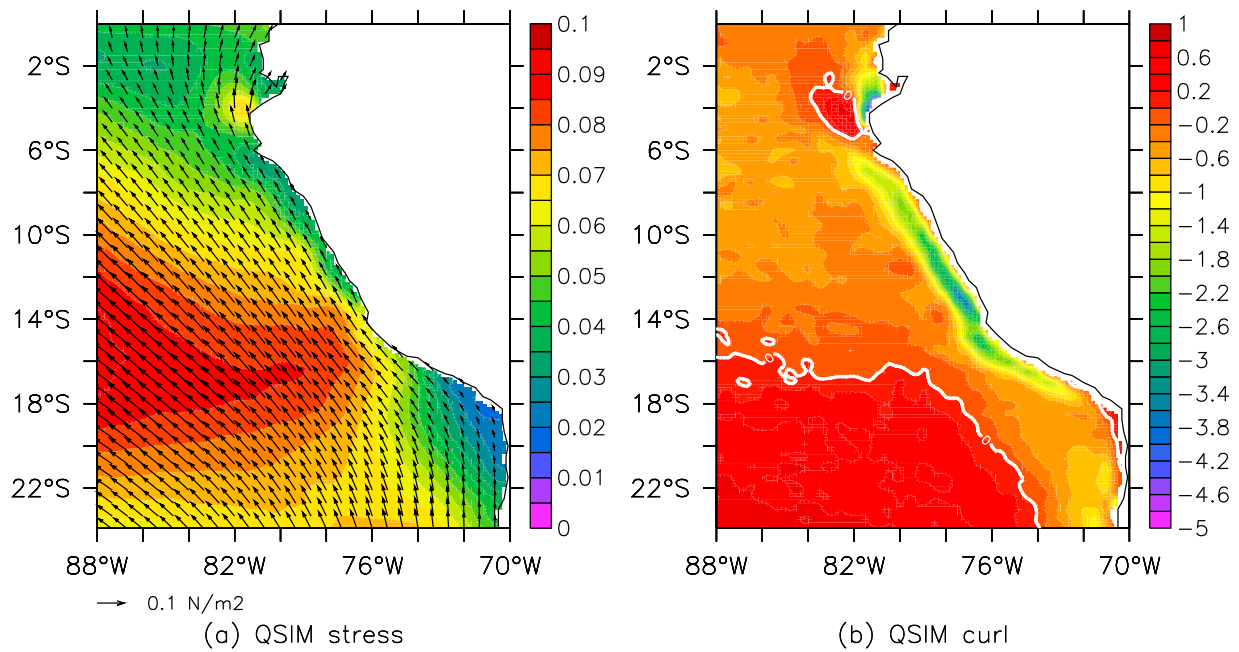


Figure 1. (a) Mean wind stress intensity and direction (arrows, in N m^{-2}) and (b) mean wind stress curl (in 10^{-7} N m^{-3}) from QSIM. The white isoline in Figure 1b denotes the position of the wind stress curl zero line.

shows strongly negative values (lower than $-1.10 \cdot 10^{-7} \text{ N m}^{-3}$), with a maximum of $-7.10 \cdot 10^{-7} \text{ N m}^{-3}$ near 14°S induced by the cape effect of the Paracas Peninsula.

3.1.2. Sea Surface Temperature

[18] Resulting mean sea surface temperature (hereafter SST) from QSIM is compared to satellite high-resolution data in Figure 2. We clearly see the signature of the coastal upwelling in both maps. However, simulated SST is colder than the observed one almost everywhere. For instance, the 20°C isotherm in Pathfinder (Figure 2b) can be superimposed with the 19°C isotherm in QSIM (Figure 2a). On average a cold bias of -1.75°C is observed between QSIM and observations (Figure 2c), except near the Paracas Peninsula where the modeled upwelling remains a little too

weak. Note that SST is partially restored to the COADS climatology in our forced simulation. Comparing COADS and Pathfinder SST leads to the same patterns than the ones depicted in Figure 2c and to an averaged cold bias of -1.23°C (not shown). Hence the model large-scale cold bias can mainly be explained by the relaxation to COADS climatology and not by a misrepresentation of the upwelling dynamics, and affects little the biological processes [Echevin *et al.*, 2008].

3.1.3. Surface Currents

[19] A data set of near-surface ($\sim 15 \text{ m}$ depth) current observations derived from satellite-tracking drifting buoys is used to evaluate simulated mean surface velocities (Figure 3). The offshore intensities are in qualitative agreement with

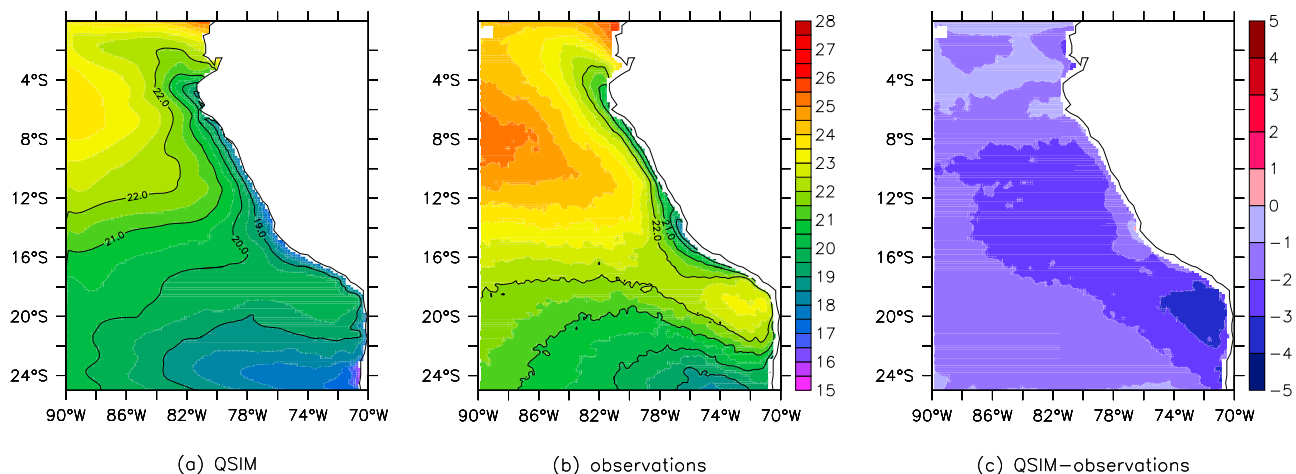


Figure 2. Mean sea surface temperature (SST) (in $^\circ\text{C}$) for (a) QSIM and (b) Pathfinder AVHRR [Kilpatrick *et al.*, 2001]. (c) Differences between model simulation and observations (in $^\circ\text{C}$). Contours are from 19°C to 22°C every 1°C .

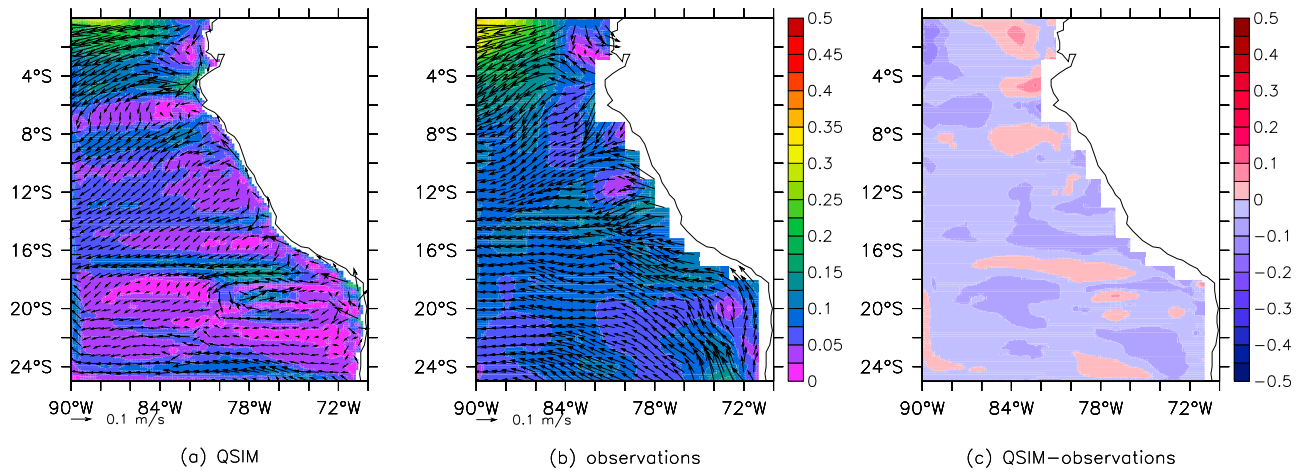


Figure 3. Mean near-surface (~ 15 m) current intensity (m s^{-1}) and direction (arrows every four model grid points) for (a) QSIM and (b) the Global Drifter Program data set based on satellite-tracked drifting buoy observations [Lumpkin and Garraffo, 2005]. (c) Differences between model and observations (in m s^{-1}).

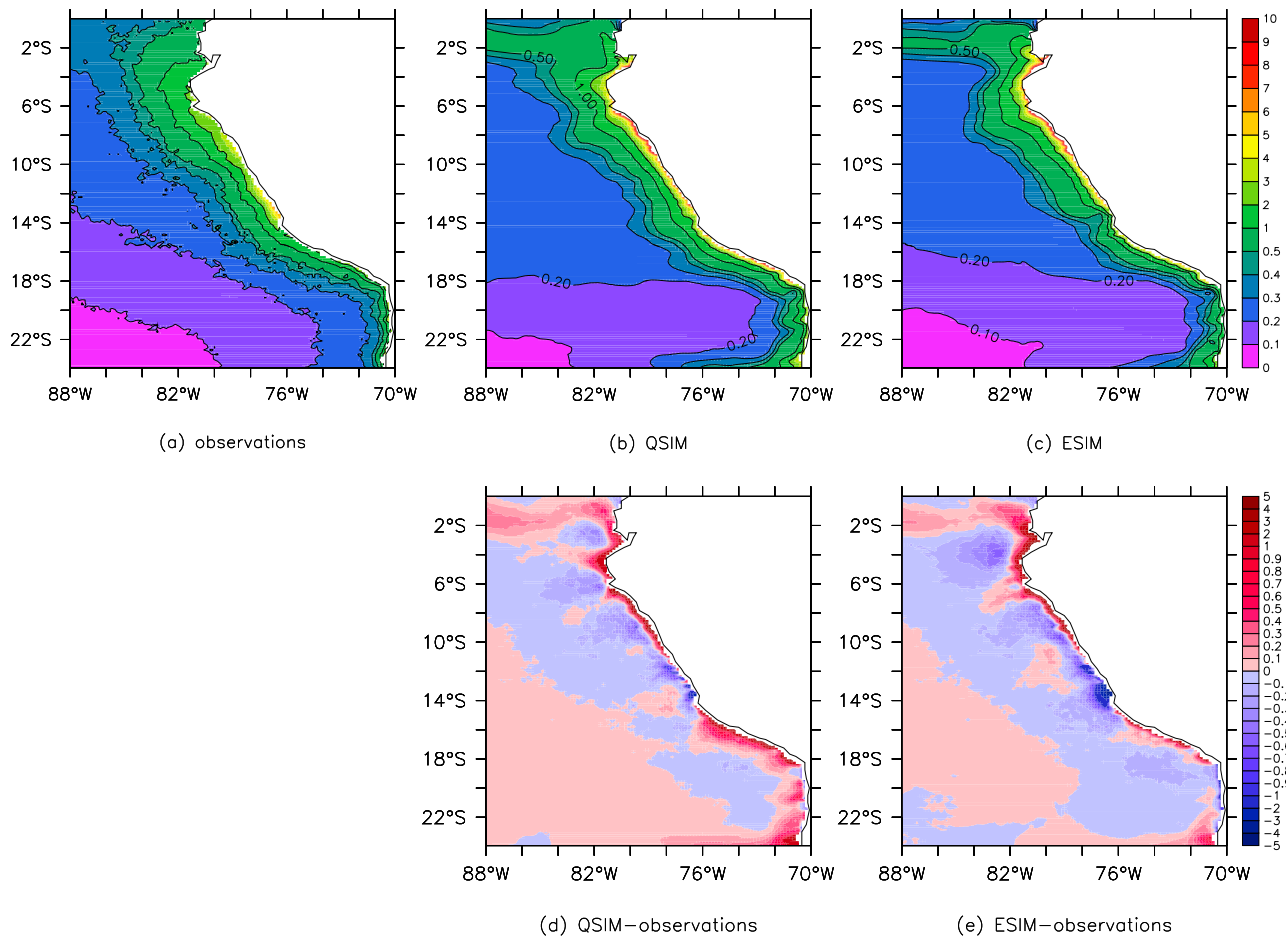


Figure 4. Mean surface chlorophyll *a* concentration (in mg Chl m^{-3}) for (a) SeaWiFS satellite data [Behrenfeld and Falkowski, 1997], (b) QSIM, and (c) ESIM. Contours of 0.2, 0.3, 0.4, 0.5, 1, and 2 mg Chl m^{-3} are represented. Differences between (d) QSIM and (e) ESIM and observations (in mg Chl m^{-3}).

Table 1. Average Estimates of Surface Chlorophyll Concentration, Primary Production, Extent of Productive Zone, Vertical Velocity, and Wind Stress Intensity and Curl From QSIM, ESIM, and QncSIM Model Simulations and Satellite [Behrenfeld and Falkowski, 1997] and in Situ Observations [Messié et al., 2009] (for Primary Production)^a

	Simulations			Differences		Observations	
	QSIM	ESIM	QncSIM	QSIM-ESIM	InSitu	Satellite	InSitu
Surface chlorophyll (mg Chl m^{-3})	4 (2.7)	3.6 (1.5)	3 (1.4)	10% (80%)	35% (98%)	3 (2.7)	3.8 (3.3)
Extent of the productive zone (km)	158 (140)	137 (66)	144 (63)	15% (112%)	10% (122%)	166 (131)	222 (190)
Primary production ($\text{g C m}^{-2} \text{ yr}^{-1}$)	448 (419)	410 (309)	391 (294)	9% (35.5%)	15% (42%)	954 (979)	570
Wind stress intensity (N m^{-2})	0.045 (0.06)	0.045 (0.06)	0.06 (0.08)	2% (10%)	-26% (-18%)		
Wind stress curl (10^{-7} N m^{-3})	-1.5 (-2)	-0.4 (-0.7)	-0.5 (-0.6)	236% (177%)	200% (275%)		
Vertical velocities 0–100 km offshore (m d^{-1})	0.089 (0.082)	0.089 (0.091)	0.119 (0.122)	0.5% (-10%)	-25% (-33%)		
Vertical velocities 100–200 km offshore (m d^{-1})	0.018 (0.09)	0.02 (-0.011)	0.003 (-0.015)	800% (-)	500% (-)		

^aValues are obtained by averaging in a 100 km coastal band or between 100 and 200 km offshore, from 6°S to 16°S (13°S to 15°S), respectively, for the Peru (Pisco) region. Differences are expressed in percentage of the ESIM and QncSIM averages. The extent of the productive zone is estimated with the distance to the coast of the 1 mg Chl m^{-3} surface chlorophyll isoline. Negative values for vertical velocities mean downwelling. Values in parentheses are for the Pisco region.

observations, although weaker on average (an averaged difference of -3 cm s^{-1} is displayed in Figure 3c). The model adequately represents the offshoreward jets near 14°S and 18°S. In the northwest corner of the model domain, the relatively strong velocities in QSIM correspond to the eastern edge of the South Equatorial Current which flows westward between equator and 6°S with observed velocities slightly higher (up to 35 cm s^{-1} ; Figure 3b) than modeled ones ($\sim 25 \text{ cm s}^{-1}$; Figure 3a).

[20] At the surface (not shown), strong values corresponding to the Peru Coastal Current (PCC) are encountered in QSIM along the coast. Surface model velocities at 10°S and 15°S compare well with observations reported in the literature: 16 cm s^{-1} and 8 cm s^{-1} for QSIM and 14 cm s^{-1} in the work by Huyer et al. [1991] and above 10 cm s^{-1} in the work by Brink et al. [1983].

[21] A more complete description of the simulated dynamics with a similar configuration ($1/9^\circ$ resolution) can be found in the work by Penven et al. [2005].

3.1.4. Surface Chlorophyll and Primary Production

[22] The simulated surface chlorophyll *a* concentration is compared with SeaWiFS satellite observations (Figure 4). The model results show good agreement with observations. Both maps display spatial patterns typical of coastal upwelling: concentrations are maximum at the coast, reaching up to 5 mg Chl m^{-3} in the observations (Figure 4b) and up to 10 mg Chl m^{-3} in the model (Figure 4a). Concentrations decrease gradually offshore, reaching values under 1 mg Chl m^{-3} at 200–300 km from the coast. Second-order differences between model and observation also appear: the highly productive nearshore zone (with concentrations higher than 2 mg Chl m^{-3}) is narrower and values very close to the shore are much higher in the simulation. One should however be very cautious when considering remotely sensed chlorophyll values close to the coast. Indeed, the SeaWiFS inverse algorithm used to calculate surface chlorophyll from radiances tends to underestimate high concentrations [Behrenfeld and Falkowski, 1997] as it may be biased by the increasing turbidity in coastal zones [Hyde et al., 2007]. Moreover, a nearshore underestimate may be exacerbated by the frequent nearshore cloud coverage, especially in winter, which could prevent the sampling of some of the intense surface blooms.

[23] A positive bias in the northeast corner of the domain also appears. It could be explained by a possible overesti-

mation of the equatorial upwelling, also observed in several global coupled models [Aumont et al., 2002]. However, we believe that this caveat does not affect our analysis which focus on the coastal region.

[24] The simulated primary production averaged along the Peruvian coast has the same order of magnitude as estimates from previous studies (Table 1). A recent estimate of potential primary production based on in situ nitrate data and QuikSCAT winds and assuming that all the available nitrate are consumed [Messié et al., 2009] shows values ($570 \text{ g C m}^{-2} \text{ yr}^{-1}$; Table 1) slightly higher than ours ($448 \text{ g C m}^{-2} \text{ yr}^{-1}$; Table 1). Another estimate based on satellite SeaWiFS chlorophyll and satellite SST [Behrenfeld and Falkowski, 1997] is more than two times greater ($954 \text{ g C m}^{-2} \text{ yr}^{-1}$; Table 1). This discrepancy may partly be due to the cloud-filling procedure performed on satellite chlorophyll data, and to the fact that the computation of primary production is based on a global algorithm, hence not adjusted in coastal areas with high chlorophyll concentrations.

3.1.5. Cross-Shore Structure of Surface Biogeochemical Fields

[25] To go beyond the limitations inherent to satellite data, model results are also compared to surface in situ data. Cross-shore transects displayed in Figure 5 have been constructed as follows: all chlorophyll, nitrate, phosphate, silicate and a few iron data located between 6°S and 16°S have been binned as a function of distance to the coast and averaged to produce climatological transects.

[26] A strong zonal gradient with typical high values near the coast is seen in the chlorophyll transects. In situ chlorophyll values are greater than SeaWiFS and model values, but the latter are very close to the in situ observations in the 0–50 km band. Cross-shore gradients are also seen in the nutrients transects. The simulated nitrate concentrations are too high, with differences of up to $4 \mu\text{mol L}^{-1}$ from observations. This can partly be explained by an overestimation of the model dissolved oxygen concentration in the oxygen minimum zone in both this model and the global model providing boundary conditions (not shown). In such conditions, the high oxygen levels prevent denitrification to take place and subsurface nitrate concentration to decrease. However, iron being the limiting nutrient in our model [Echevin et al., 2008] and possibly in observations [Bruland et al., 2005], this overestimation of surface nitrate concen-

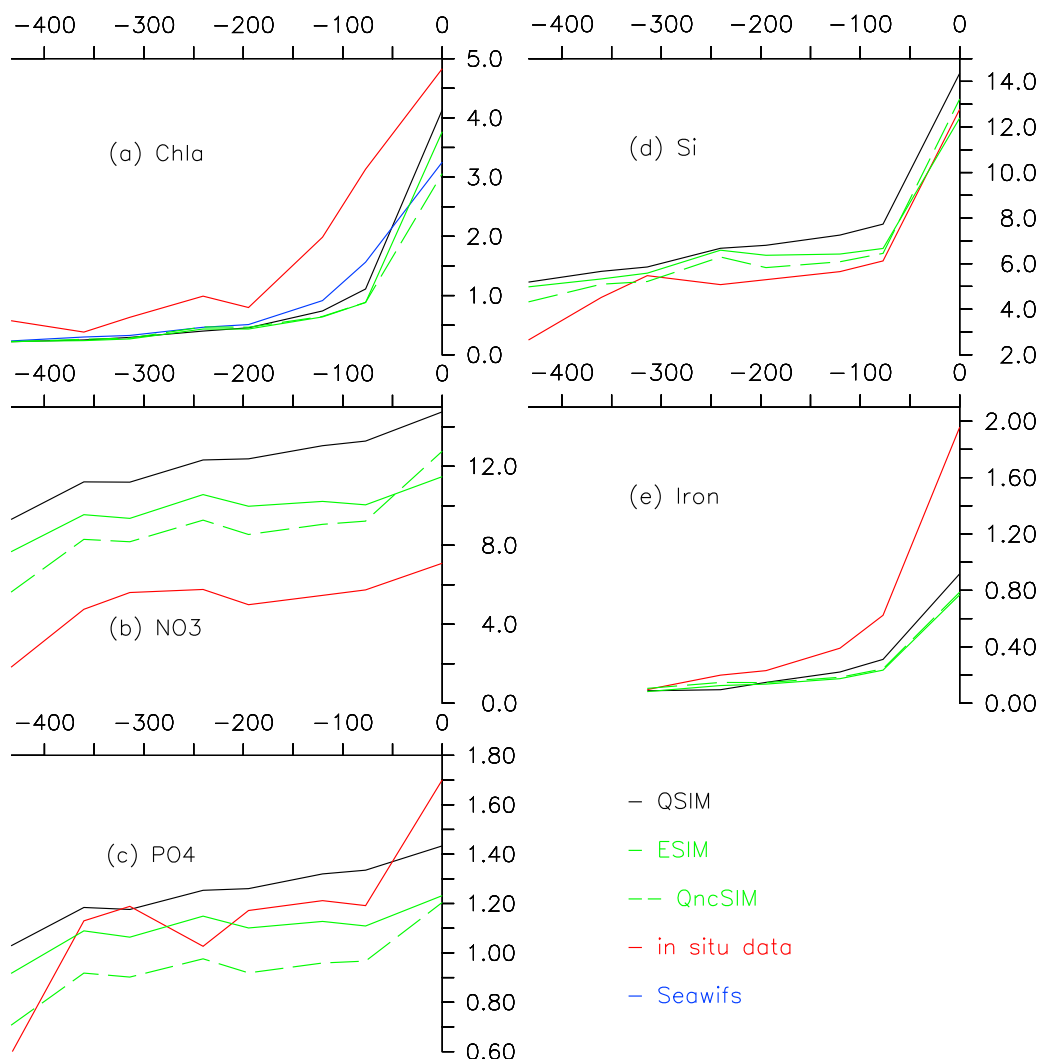


Figure 5. Cross-shore surface transects averaged along the Peruvian coast from 6°S to 16°S for surface (a) chlorophyll *a* (mg Chl m^{-3}), (b) nitrate, (c) phosphate, (d) silicate ($\mu\text{mol L}^{-1}$), and (e) iron (nmol L^{-1}) concentrations. QSIM profiles are plotted by solid black line, ESIM is plotted by solid green line, QncSIM is plotted by green dashed line, SeaWiFS chlorophyll *a* is plotted by solid blue line, and in situ IMARPE and *Bruland et al.* [2005] data are plotted by solid red line.

tration does not lead to an overestimation of primary production (see Table 1). Simulated phosphate and silicate are in better agreement with observations (Figures 5c and 5d). Simulated austral iron concentrations are lower than in situ values, which represent winter conditions in 2000.

[27] Despite the caveats previously described, our simulation is realistic enough to allow performing meaningful sensitivity experiments on the influence of the wind stress onto the biological productivity.

3.2. Sensitivity Experiments on Wind Stress Curl

[28] In the following part, simulations forced by three different wind products are analyzed. We first describe the surface forcings and their major differences.

3.2.1. Wind Stress and Curl

[29] The ERS and QuikSCAT wind products differ in many respects (spatial and temporal resolution, time period considered or the frequency of the microwave instrument), which results in the mean wind stress and curl differences

portrayed in Figure 6. Offshore, QSIM wind stresses are higher (+20% on average) than ESIM as also noted by [Croquette *et al.*, 2007]. Due to the larger coastal blind zone and to the presence of the dropoff, ESIM wind stress values extrapolated on the nearshore model grid points are artificially high (Figure 6a). The coastal band showing strongly negative wind stress curl for QSIM (Figure 1b) is smoothed in ESIM, leading to significant differences (Figure 6b): wind stress curl is more than twice higher in QSIM than in ESIM (Table 1).

[30] One may argue that ERS and QuikSCAT winds differ in too many respects to properly distinguish the effect of coastal wind stress curl in the QSIM and ESIM simulations. The effect of higher offshore wind stress and deeper mixed layer in QSIM could partially enhance the effect of the strong upwelling-favorable nearshore wind stress curl. We therefore constructed a new product based on QuikSCAT by smoothing the wind stress values in a nearshore band of

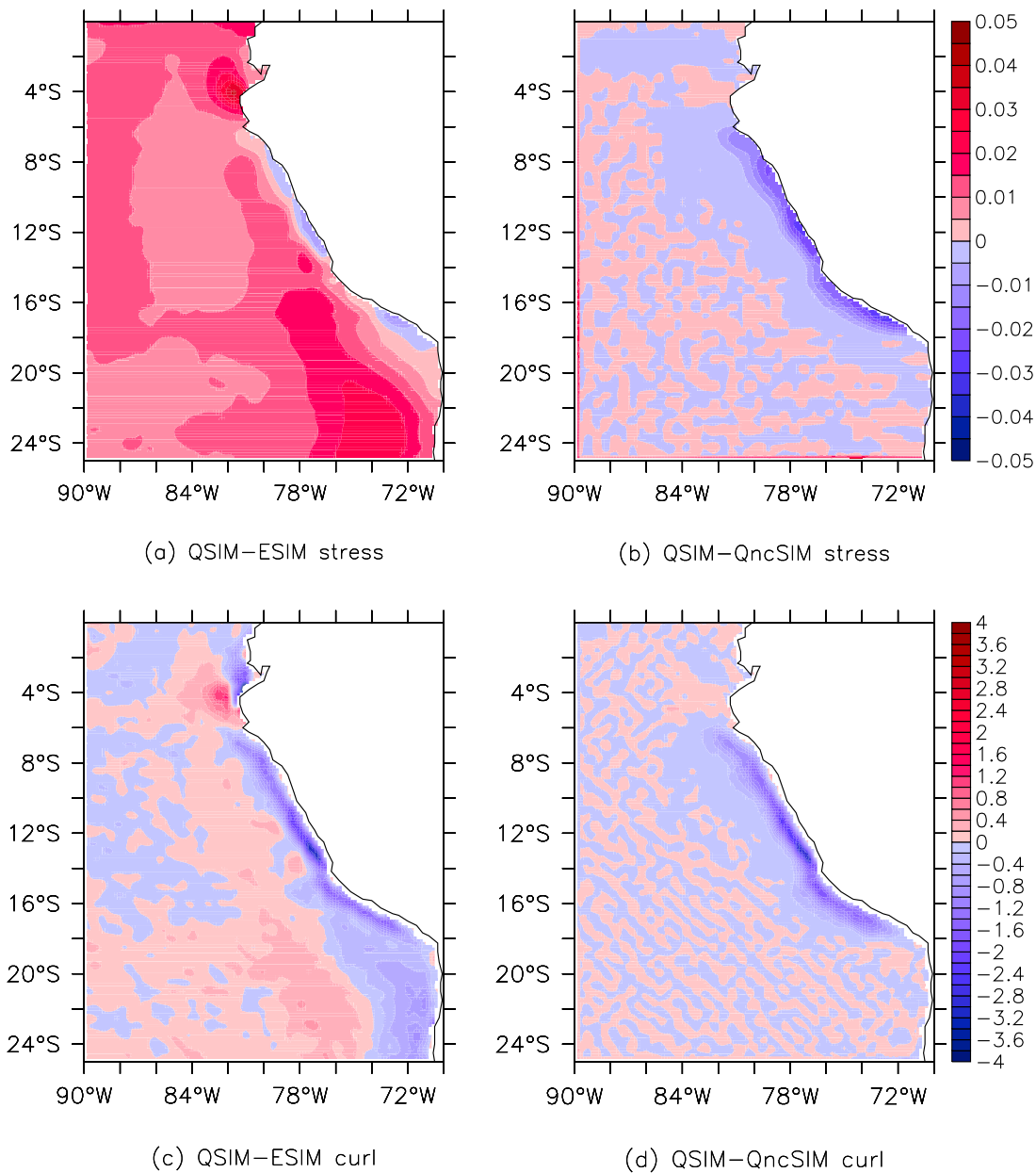


Figure 6. Wind stress differences (in Nm^{-2}) (a) between QSIM and ESIM and (b) between QSIM and QncSIM. Wind stress curl (in 10^{-7}Nm^{-3}) differences (c) between QSIM and ESIM and (d) between QSIM and QncSIM.

200 km, which reduced the dropoff and resulted in a curl not lower than $-1.10^{-7} \text{N m}^{-3}$.

[31] Wind stress and curl differences between QSIM and QncSIM are depicted in Figures 6c and 6d. QncSIM and QSIM forcings only differ in the coastal band between 6°S and 18°S. Coastal winds are stronger in QncSIM (Figure 6c) therefore wind stress curl is less negative (Figure 6d). We quantified these differences along the coast in Table 1: QncSIM wind stress is 26% higher and QSIM wind stress curl is twice negatively stronger, almost three times stronger near Pisco. More importantly, note that QncSIM nearshore average values are very close to ESIM (Table 1). In sections 3.2.2–3.2.6, the QncSIM simulation is compared to both QSIM and ESIM.

3.2.2. SST and Near-Surface Currents

[32] QSIM SST and near-surface currents have been compared to available observations in sections 3.1.2 and 3.1.3. ESIM SST and near-surface currents are very similar to QSIM (not shown). On average in the entire model domain, SST differences between QSIM and ESIM are of 0.13°C . Near Pisco (15°S), QSIM SST is closer to the observed: maximum difference from observations is 1.3°C in QSIM whereas it reaches 2.3°C in ESIM. QSIM (Figure 2a) and ESIM (not shown) near-surface currents mean differences from observations are of -0.03 m s^{-1} and -0.04 m s^{-1} , respectively. As far as surface dynamics are concerned, results from QSIM and ESIM are very similar, with a slightly more realistic SST in QSIM.

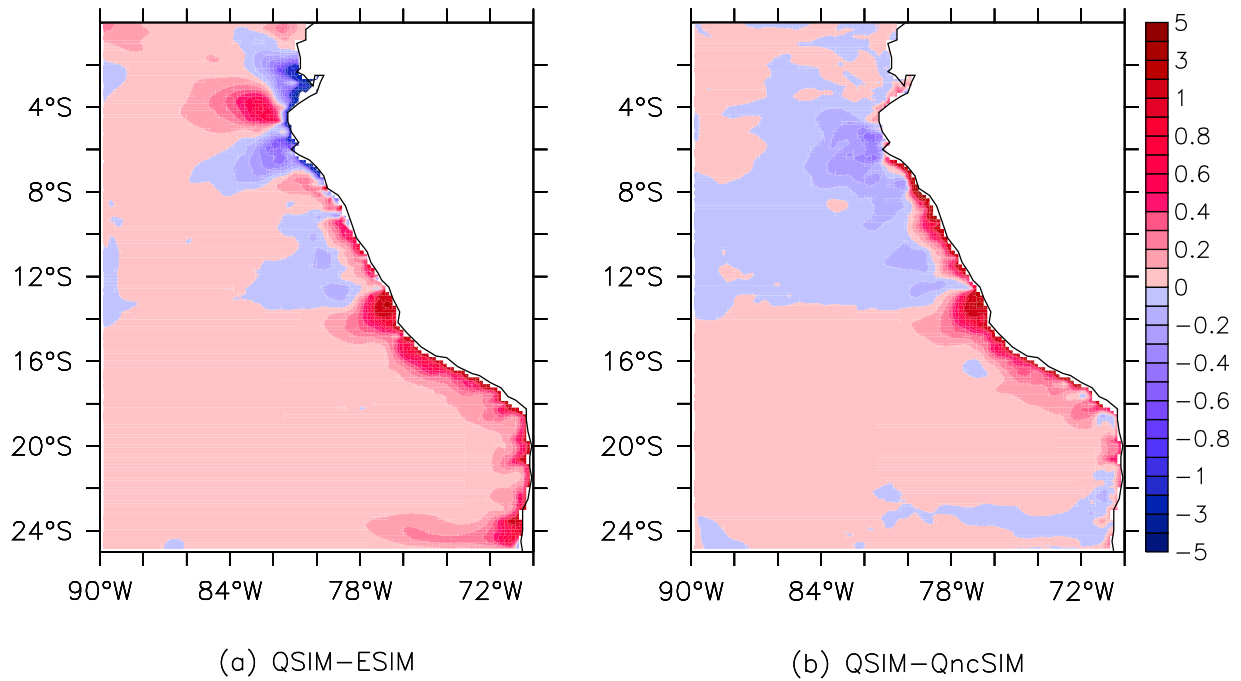


Figure 7. Surface chlorophyll *a* (in mg Chl m^{-3}) differences (a) between QSIM and ESIM and (b) between QSIM and QncSIM.

3.2.3. Surface Chlorophyll

[33] Differences between QSIM and ESIM (resp. QncSIM) in mean surface chlorophyll are displayed in Figure 7. In both cases, QSIM is more productive. The greatest differences

(0–5 mg Chl m^{-3}) are encountered near the coast south of 12°S with maximum values of 4 and 7 mg Chl m^{-3} off Pisco for QSIM-ESIM and QSIM-QncSIM differences, respectively. The large-scale dipole pattern between 2°S

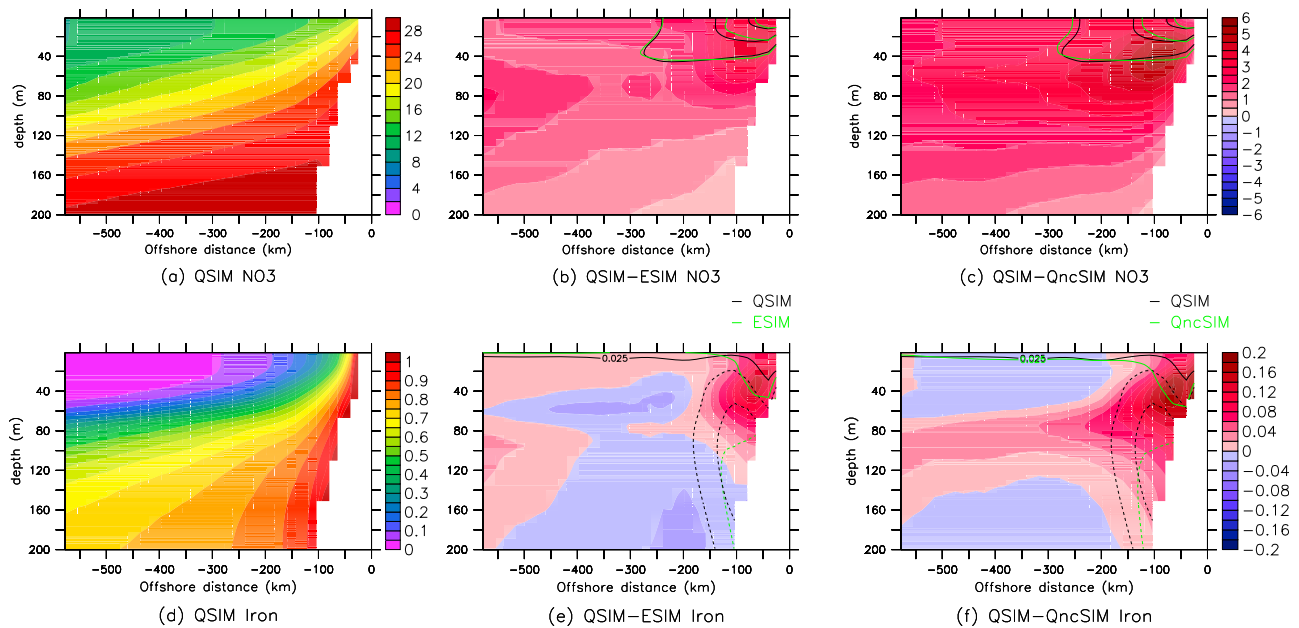


Figure 8. (a–f) Cross-shore sections averaged along the Peruvian coast from 8°S to 16°S for nitrate (Figure 8a) (in $\mu\text{mol L}^{-1}$) and iron (Figure 8d) (in nmol L^{-1}) concentrations for QSIM. Differences in nitrate concentration between QSIM and ESIM (Figure 8b) and QSIM and QncSIM (Figure 8c). Differences in iron concentration between QSIM and ESIM (Figure 8e) and QSIM and QncSIM (Figure 8f). Contours in Figures 8b and 8c (Figures 8e and 8f) correspond to QSIM (in black) and ESIM and QncSIM (in green) chlorophyll 0.5, 1, and 2 mg Chl m^{-3} isolines (alongshore currents -0.05 , -0.025 , and 0 m s^{-1} isolines).

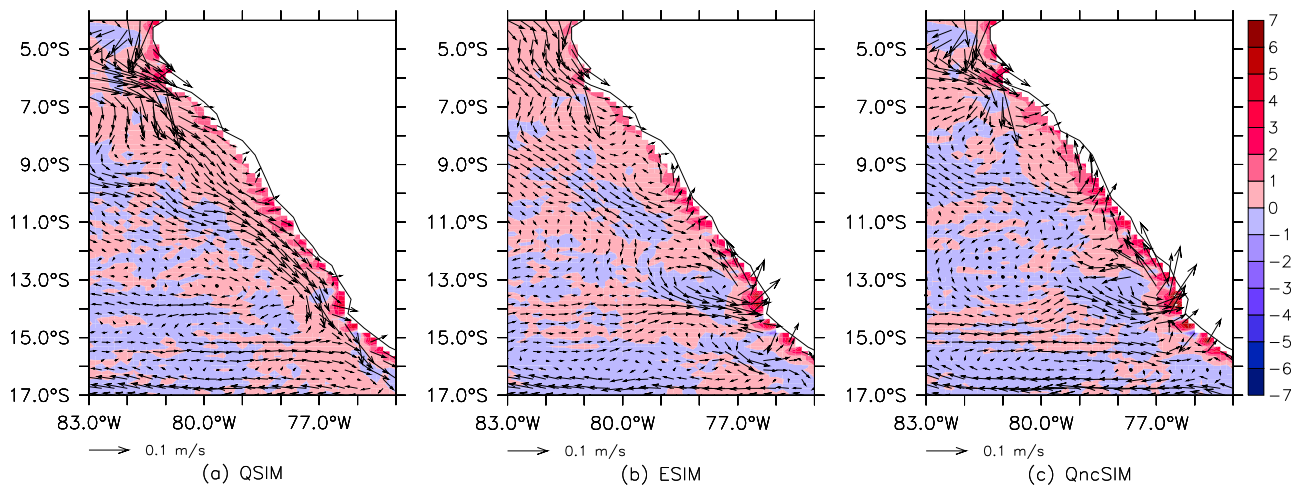


Figure 9. Mean horizontal circulation (arrows every two model grid points, in m s^{-1}) and vertical velocities (color scale, in m d^{-1}) at 60 m depth obtained from (a) QSIM, (b) ESIM, and (c) QncSIM.

and 8°S in Figure 7a is related to mesoscale patterns in wind stress curl differences (Figure 6c) which will not be further investigated in this study.

[34] When averaged in a 100 km wide coastal box between 6°S and 16°S (Table 1), the chlorophyll concentration is increased by 10% (35%) in QSIM with respect to ESIM (QncSIM), and primary production is increased by 9% (15%). In the Pisco region (13°S–15°S, from 0 to 100 km offshore), the change is even more drastic: +80% (98%) for chlorophyll and +35.5% (42%) for primary production.

[35] We also computed the width of the productive zone, defined as the distance from the coast of the 1 mg Chl m^{-3} surface chlorophyll isoline. Whereas the mean width (averaged along the coast between 6°S and 16°S) is comparable in all simulations (Table 1), in the Pisco region (13°S–15°S) it is drastically reduced in ESIM (66 km) and QncSIM (63 km) when compared to QSIM (140 km) or satellite data (131 km). The width of the productive zone derived from in situ data is higher (190 km) than the previous estimates, but one should keep in mind that in situ observations are relatively scarce in this region.

[36] In terms of surface chlorophyll and primary production, these results show that simulation driven with QuikSCAT forcing produce more realistic patterns and values than with ERS forcing.

3.2.4. Nutrient Availability

[37] Surface nutrient concentrations are found more abundant in QSIM when averaged over the Peruvian coast (Figure 5) with differences of 1.8 (1.9), 0.1 (0.2), 0.5 (0.3) $\mu\text{mol L}^{-1}$ and 0.01 (0.005) nmol L^{-1} for nitrate, phosphate, silicate and iron, respectively, when compared to ESIM (QncSIM). Iron concentration differences are very weak at the surface as this nutrient is almost entirely consumed by biological activity in all simulations.

[38] Higher concentrations of nitrate and iron are also found in subsurface waters (Figure 8). Maximum differences are found at 40 m depth and ~100 km offshore (Figures 8b, 8c, 8e, and 8f) with differences between QSIM and ESIM (resp. QncSIM) of up to 4 (resp. 5) $\mu\text{mol L}^{-1}$ for nitrate and 0.15 (resp. 0.2) nmol L^{-1} for iron. The coastal euphotic zone is therefore significantly nutrient-richer in QSIM, stimulating plankton growth and accumulation. Note that nitrate enrichment is seen as far as 600 km offshore while iron enrichment occurs mainly on the shelf and slope. The dynamical features the circulation responsible for this modification of nutrient availability are investigated in section 3.2.5.

3.2.5. Circulation Patterns

[39] Mean vertical velocities at 60 m depth portrayed in Figure 9 show similar patterns in the three simulations, with a coastal intensification of upward velocities. When aver-

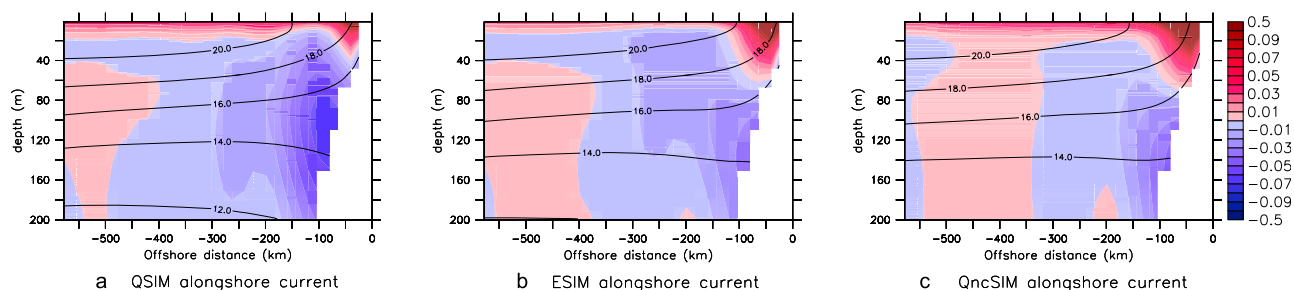


Figure 10. Cross-shore sections averaged over the Peruvian coast (6°S to 16°S) of alongshore currents for (a) QSIM, (b) ESIM, and (c) QncSIM in m s^{-1} . Contours represent the 12°C, 14°C, 16°C, 18°C, and 20°C isotherms.

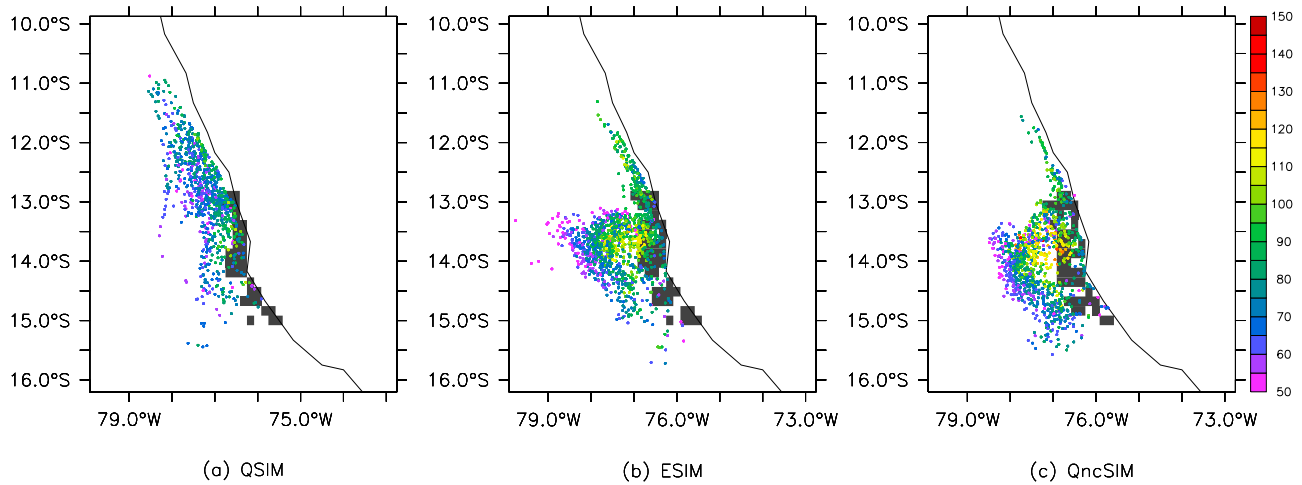


Figure 11. Position and depth (color scale, in m) of the water parcels 1 month before being upwelled in the Pisco area for (a) QSIM, (b) ESIM, and (c) QncSIM. Black squares indicate where the parcels were upwelled at depths between 50 and 60 m.

aged between 40 m and 60 m depth and within 100 km from the coast, vertical velocities are 25% higher in QncSIM between 6°S and 16°S (33% higher off Pisco) whereas vertical velocities in ESIM are quite similar (10% difference off Pisco) to those in QSIM (Table 1). These differences are consistent with wind stress differences. Further offshore in the 100–200 km coastal range, QSIM vertical velocities are 9 (6) times stronger than ESIM (QncSIM) ones (Table 1). Ekman pumping, enhanced in QSIM, may therefore partly explain the upwelling of nutrient-replete waters in QSIM described in section 3.2.3.

[40] Besides, ESIM and QncSIM horizontal circulations contrast with QSIM (Figure 9). A well-defined poleward alongshore flow can be identified as the Peru Chile Undercurrent (PCUC) in QSIM (Figure 9a). This feature is replaced by a cross-shore flow originating from offshore in ESIM (Figure 9b) and QncSIM (Figure 9c), transporting potentially nutrient-deplete offshore waters in the upwelling area.

[41] Cross-shore sections of the alongshore component of the flow also show quite different patterns (Figure 10). The

equatorward coastal current is more intense and thicker in ESIM (Figure 10b) than in QSIM (Figure 10a) and even more so in QncSIM (Figure 10c). This is related to the rather flat isotherms offshore (e.g., the 16°C isotherms in Figure 10), which are little displaced by Ekman upward pumping in ESIM and QncSIM and slope steeply upward near the coast due to the intense coastal divergence. The splitting of isotherms toward the shore confirms the presence of the PCUC near 100 m depth in QSIM, while the undercurrent is weaker and flows deeper (~140 m depth) in ESIM and QncSIM. The depth and velocity of this undercurrent in QSIM are closer to observations than ESIM, as Huyer [1980] measured a PCUC flowing at 100–150 m with a maximum velocity on the slope of 15 cm s^{-1} .

[42] The PCUC has been recognized as a major source of nutrient-rich waters for the upwelling area [Gunther, 1936; Fonseca, 1989]. In the QSIM simulation it acts as a nutrient stream, as the upper part of the PCUC is colocated with anomalies of nitrate (Figures 8b and 8c) and iron concen-

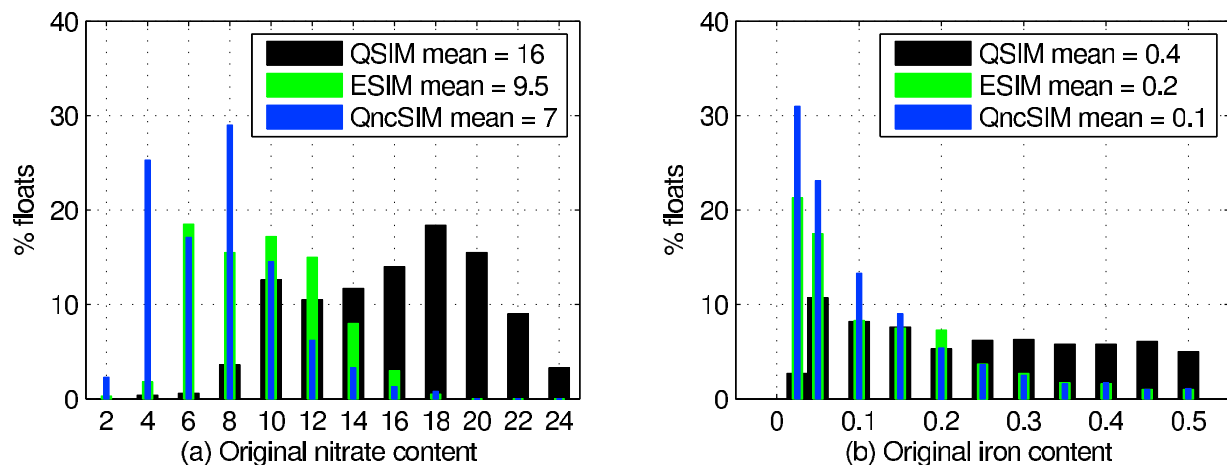


Figure 12. Histograms of (a) nitrate and (b) iron content of water parcels 1 month before they were upwelled in the Pisco area for QSIM (black bars), ESIM (green bars), and QncSIM (blue bars).

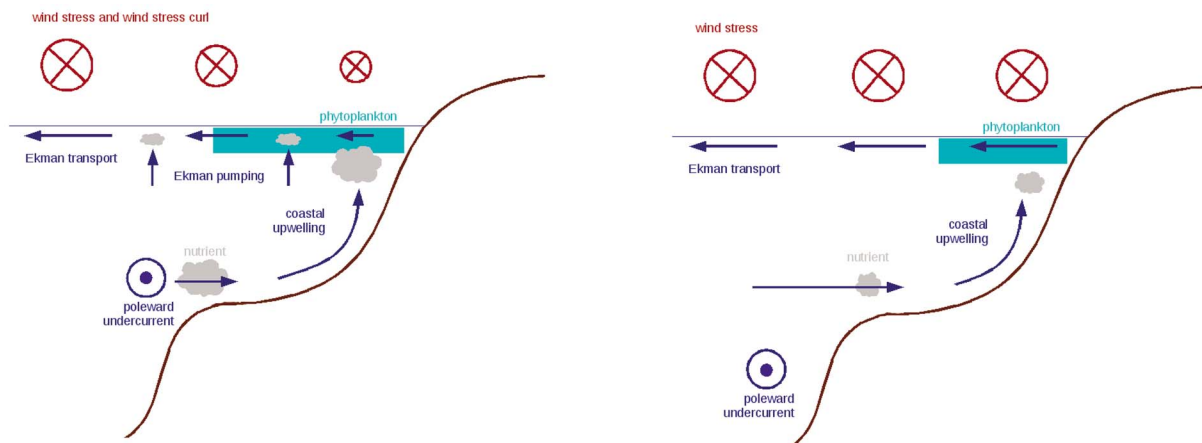


Figure 13. (left and right) Schematic representation of the mechanisms linking wind stress curl to primary production. Alongshore wind stress (in red) decreases in the dropoff zone (from ~ 200 km to the coast) leading to negative wind stress curl (Figure 13, left). Ekman transport (horizontal arrows in blue) is related to wind stress, and Ekman pumping (vertical arrows in blue) is related to wind stress curl. The poleward undercurrent driven by wind stress curl transports nutrient-rich waters to be coastally upwelled. Phytoplankton grows and accumulates in the coastal euphotic zone. In the absence of wind stress curl, Ekman divergence is stronger at the coast and Ekman pumping is nonexistent. The undercurrent flows more deeply and is no longer the source of upwelled waters, which are consequently less nutrient-rich.

tration (Figures 8e and 8f). We examine in section 3.2.6 the characteristics of the upwelled waters in all simulations.

3.2.6. Origin of Upwelled Waters

[43] We reconstructed the trajectories of water parcels backward in time using a lagrangian tool (see section 2.4). We chose to focus on the characteristics of the source waters before they are upwelled off Pisco. We therefore released artificial floats at 50–60 m depth where vertical velocities are greater than 1 m d^{-1} . These floats follow the water parcels bound to be upwelled in the coastal euphotic zone. Results show that the origin of source waters are quite different in the three simulations (Figure 11): upwelled waters in QSIM predominantly come from a more northern and nearshore region than in ESIM and QncSIM. The initial depths are comparable, 80 m on average for all simulations, and slightly greater in ESIM and QncSIM (Figure 11). Nitrate and iron contents are strikingly different (Figure 12) with averaged concentrations 1.5 (2) and 2 (4) times higher, respectively, in QSIM when compared to ESIM (QncSIM). These results indicate that richer rather than deeper waters are upwelled in QSIM.

[44] Two mechanisms explain the QSIM richness in nutrients. First, water masses have been displaced upward by Ekman pumping in the nearshore regions, thus source waters in the 60–80 m depth range are richer in nutrient. Secondly, a shallow, continuous undercurrent transports the source waters along the shelf and slope, allowing them to accumulate iron.

4. Discussion and Conclusions

[45] We pointed out that the presence of a negative wind stress curl pattern in the QuikSCAT forcing has intensified coastal primary production through (1) the upwelling of nutrients through Ekman pumping and (2) the transport of iron into the euphotic zone by a shallow, continuous pole-

ward alongshore undercurrent (Figure 13). Furthermore, the curl is associated to a decrease of the alongshore wind component at the coast in QuikSCAT with respect to ERS, leading to a decrease in coastal upwelling forced by the coastal divergence of Ekman flow. However, this effect may be locally overcompensated by the curl-driven upwelling in terms of nutrients vertical flux, particularly in regions of strong curl such as near Pisco (15°S).

[46] Several previous studies have focused on the possible compensation between coastal divergence and Ekman pumping and their conclusions differ depending on the method used. *Pickett and Paduan* [2003] and *Enriquez and Firehe* [1995] used an Ekman current model and wind estimates from atmospheric models and argued the Ekman pumping associated with large curl is comparable in magnitude with the effect of Ekman coastal divergence. *Fennel and Lass* [2007], using a simple analytical model, concluded that strong wind stress curl substantially intensifies the upwelling even if alongshore winds decrease. On the other hand, *Capet et al.* [2004] used a California current system regional model forced by wind stress products with and without strong wind dropoff, and found that the intensity of the dynamical upwelling (diagnosed with lagrangian floats) decreased in the strong dropoff case. However, their case study was rather extreme as their imposed wind dropoff resulted in an alongshore wind stress 2 to 4 times weaker than observations from a coastal mooring, hence in a very weak coastal divergence.

[47] Although the wind stress curl changes are mainly seen in a coastal range (from coast to ~ 200 km offshore; Figure 6), a drastic change of thermocline (Figure 10) and nutricline and ironcline (Figure 8) depth is observed away from the coast. A dynamical adjustment to the wind forcing took place during the 10 year spin-up phase, leading to an uplifting of the thermocline (and nutricline) away from the shore by westward propagating eddies and Rossby waves

(not shown). This explains the accumulation of nutrients in the surface layers away from the coast in the case of strong nearshore Ekman pumping.

[48] Other processes related to the wind intensity may influence the surface chlorophyll concentration. Stronger alongshore coastal winds (such as in ESIM and QncSIM) induce a moderate deepening of the coastal mixed layer. This may reduce the surface concentration of phytoplankton by a dilution effect and limit its growth by a light limitation effect [Echevin *et al.*, 2008].

[49] The dynamical impact of the curl on the undercurrent may occur in other EBUS where strong coastal wind stress curl are observed [Risien and Chelton, 2008]. Theoretically, Sverdrup's [1947] transport balance relates the vertically integrated meridional mass transport in the interior ocean to the open ocean wind stress curl. A theoretical analysis by Pedlosky [1974] suggests that a poleward undercurrent along an eastern boundary is favored by positive (in the Northern Hemisphere) wind stress curl along the coast. Data from the California current system also indicates that the poleward undercurrent observed along the West Coast of North America may be driven locally by positive wind stress curl [Nelson, 1977]. More recently, Marchesiello *et al.* [2003] showed that regional model and Sverdrup transports are consistent in the California current system. The biogeochemical response to the presence of wind stress curl and nutrient transport by the undercurrent is therefore likely to occur in other EBUS, however modulated by inherent local characteristics such as nutrient limitations.

[50] We diagnosed a change in the nearshore subsurface circulation by explicitly simulating the coupling of dynamics and biogeochemistry in the upwelling system. Differences in dynamical patterns could also be found by analyzing SST instead of surface chlorophyll. However, the SST from forced simulations is always partially restored to observed climatologies or data sets to correct potential surface heat fluxes biases. Modeled SST patterns would therefore be biased and less reliable (not shown). Thus, despite the uncertainties and nonlinearities inherent to the parameterization of ecosystem models, the present study also suggests that surface chlorophyll obtained from coupled dynamical-biogeochemical simulations may be an interesting tool that can help assessing the wind-forced nearshore ocean circulation.

[51] Even though QuikSCAT is able to retrieve part of the cross-shore wind gradient not captured by ERS [Croquette *et al.*, 2007], the existence of the 25 km wide coastal blind zone sampling may induce large errors. Thus, regional wind products blending satellite observations and fields from high-resolution regional atmospheric models [Chao *et al.*, 2003] are likely to become a useful product for the realistic modeling of dynamical and biogeochemical processes in upwelling systems.

[52] **Acknowledgments.** This study formed part of the Ph.D. dissertation of A. Albert funded by a scholarship from Ministère de l'Éducation Supérieure et de la Recherche. We would like to thank J. Ledesma from Instituto del Mar de Peru, Lima, for providing the in situ biogeochemical data. Model simulations were performed on the supercomputer NEC-SX8 (brodie) from Institut du Développement et des Ressources en Informatique Scientifique. Financial support was provided by Institut de Recherche pour le Développement for V. Echevin and O. Aumont, by Centre National de la

Recherche Scientifique for M. Lévy, and by the Peru Ecosystem Projection Scenarios ANR-VCMS08 project.

References

- Aumont, O., and L. Bopp (2006), Globalizing results from ocean in situ iron fertilization studies, *Global Biogeochem. Cycles*, **20**, GB2017, doi:10.1029/2005GB002591.
- Aumont, O., S. Belviso, and P. Monfray (2002), Dimethylsulfoniopropionate (DMSP) and dimethylsulfide (DMS) sea surface distributions simulated from a global three-dimensional ocean carbon cycle model, *J. Geophys. Res.*, **107**(C4), 3029, doi:10.1029/1999JC000111.
- Aumont, O., E. Maier-Reimer, S. Blain, and P. Monfray (2003), An ecosystem model of the global ocean including Fe, Si, P colimitations, *Global Biogeochem. Cycles*, **17**(2), 1060, doi:10.1029/2001GB001745.
- Behrenfeld, M. J., and P. G. Falkowski (1997), Photosynthetic rates derived from satellite-based chlorophyll concentrations, *Limnol. Oceanogr.*, **42**(1), 1–20.
- Blanke, B., C. Roy, P. Penven, S. Speich, J. McWilliams, and G. Nelson (2002), Linking wind and interannual upwelling variability in a regional model of the southern Benguela, *Geophys. Res. Lett.*, **29**(24), 2188, doi:10.1029/2002GL015718.
- Blanke, B., S. Speich, A. Bentamy, C. Roy, and B. Sow (2005), Modeling the structure and variability of the southern Benguela upwelling using QuikSCAT wind forcing, *J. Geophys. Res.*, **110**, C07018, doi:10.1029/2004JC002529.
- Brink, K. H., D. Halpern, A. Huyer, and R. L. Smith (1983), The physical environment of the Peruvian upwelling system, *Prog. Oceanogr.*, **12**, 185–305.
- Bruland, K. W., E. L. Rue, G. J. Smith, and G. R. DiTullio (2005), Iron, macronutrients and diatom blooms in the Peru upwelling regime: Brown and blue waters of Peru, *Mar. Chem.*, **93**, 81–103.
- Capet, X. J., P. Marchesiello, and J. C. McWilliams (2004), Upwelling response to coastal wind profiles, *Geophys. Res. Lett.*, **31**, L13311, doi:10.1029/2004GL020123.
- Carr, S. D., X. J. Capet, J. C. McWilliams, J. T. Pennington, and F. P. Chavez (2008), The influence of diel vertical migration on zooplankton transport and recruitment in an upwelling region: Estimates from a coupled behavioral-physical model, *Fish. Oceanogr.*, **17**, 1–15.
- Chao, Y., Z. Li, J. C. Kindle, J. D. Paduan, and F. P. Chavez (2003), A high-resolution surface vector wind product for coastal oceans: Blending satellite scatterometer measurements with regional mesoscale atmospheric model simulations, *Geophys. Res. Lett.*, **30**(1), 1013, doi:10.1029/2002GL015729.
- Colas, F., X. Capet, J. McWilliams, and A. Shchepetkin (2008), El Niño off Peru: A numerical study, *Prog. Oceanogr.*, **79**, 138–155.
- Croquette, M., G. Eldin, C. Grados, and M. Tamayo (2007), On differences in satellite wind products and their effects in estimating coastal upwelling processes in the south-east Pacific, *Geophys. Res. Lett.*, **34**, L11608, doi:10.1029/2006GL027538.
- DaSilva, A., C. Young, and S. Levitus (1994), *Atlas of Surface Marine Data 1994*, vol. 1, *Algorithms and Procedures*, NOAA, Silver Spring, Md.
- Echevin, V., O. Aumont, J. Ledesma, and G. Flores (2008), The seasonal cycle of surface chlorophyll in the Peruvian upwelling system: A modeling study, *Prog. Oceanogr.*, **79**, 167–176.
- Edwards, K. A., A. M. Rogerson, C. D. Winant, and D. P. Rogers (2001), Adjustment of the marine atmospheric boundary layer to a coastal cape, *J. Atmos. Sci.*, **58**, 1511–1528.
- Enriquez, A. G., and C. Firehe (1995), Effects of wind stress and wind stress curl variability on coastal upwelling, *J. Phys. Oceanogr.*, **25**, 1651–1671.
- Fennel, W., and H. U. Lass (2007), On the impact of wind curls on coastal currents, *J. Mar. Syst.*, **68**, 128–142.
- Fonseca, T. (1989), An overview of the poleward undercurrent and upwelling along the Chilean coast, in *Poleward Flows Along Eastern Ocean Boundaries*, vol. 34, edited by R. T. Barber, pp. 203–218, Springer, New York.
- Gunther, E. (1936), A report on oceanographic investigations in the Peru Coastal Current, *Discovery Rep.*, **13**, 107–206.
- Huyer, A. (1980), The offshore structure and subsurface expressions of sea level variations off Peru, 1976–1977, *J. Phys. Oceanogr.*, **10**, 1755–1768.
- Huyer, A., M. Knoll, T. Paluszkiwicz, and R. L. Smith (1991), The Peru Undercurrent: A study of variability, *Deep Sea Res., Part A*, **39**, 247–279.
- Hyde, K. J. W., J. E. O'Reilly, and C. A. Oviatt (2007), Validation of SeaWiFS chlorophyll *a* in Massachusetts Bay, *Cont. Shelf Res.*, **27**, 1677–1691.
- Jin, X., C. Dong, J. Kurian, J. C. McWilliams, D. Chelton, and Z. Li (2009), SST-wind interaction in coastal upwelling: Oceanic simulation with empirical coupling, *J. Phys. Oceanogr.*, **39**, 2957–2970.

- Kilpatrick, K. A., G. P. Podesta, and R. Evans (2001), Overview of the NOAA/NASA advanced very high resolution radiometer Pathfinder algorithm for sea surface temperature and associated matchup database, *J. Geophys. Res.*, **106**, 9179–9197.
- Lumpkin, R., and Z. Garraffo (2005), Evaluating the decomposition of tropical Atlantic drifter observations, *J. Atmos. Oceanic Technol.*, **22**, 1415–1442.
- Marchesiello, P., J. C. McWilliams, and A. F. Shchepetkin (2003), Equilibrium structure and dynamics of the California current system, *J. Phys. Oceanogr.*, **33**, 753–783.
- Messié, M., J. Ledesma, D. D. Kolber, R. P. Michisaki, and F. P. Chavez (2009), Potential new production in four eastern boundary upwelling systems, *Prog. Oceanogr.*, **83**, 151–158.
- Nelson, C. S. (1977), Wind stress and wind stress curl over the California current, *Tech. Rep. NMFS SSRF-714*, NOAA, Silver Spring, Md.
- Pedlosky, J. (1974), Longshore currents, upwelling and bottom topography, *J. Phys. Oceanogr.*, **4**, 214–226.
- Penven, P., V. Echevin, J. Pasapera, F. Colas, and J. Tam (2005), Average circulation, seasonal cycle, and mesoscale dynamics of the Peru Current System: A modeling approach, *J. Geophys. Res.*, **110**, C10021, doi:10.1029/2005JC002945.
- Pickett, M. H., and J. D. Paduan (2003), Ekman transport and pumping in the California Current based on the U.S. Navy's high-resolution atmospheric model (COAMPS), *J. Geophys. Res.*, **108**(C10), 3327, doi:10.1029/2003JC001902.
- Renault, L., B. Dewitte, M. Falvey, R. Garreaud, V. Echevin, and F. Bonjean (2009), Impact of atmospheric coastal jet off central Chile on sea surface temperature from satellite observations (2000–2007), *J. Geophys. Res.*, **114**, C08006, doi:10.1029/2008JC005083.
- Risien, C. M., and D. B. Chelton (2008), A global climatology of surface wind and wind stress fields from eight years of QuikSCAT scatterometer data, *J. Phys. Oceanogr.*, **38**, 2379–2413, doi:10.1175/2008JPO3881.1.
- Shchepetkin, A. F., and J. C. McWilliams (2005), The regional oceanic modeling system (ROMS): A split-explicit, free-surface, topography-following-coordinate ocean model, *Ocean Modell.*, **9**, 347–404.
- Sverdrup, H. U. (1947), Wind-driven currents in a baroclinic ocean: With application to the equatorial currents of the eastern Pacific, *Proc. Natl. Acad. Sci. U. S. A.*, **33**, 318–326.
- Tegen, I., and I. Fung (1995), Contribution to the atmospheric mineral aerosol load from land surface modification, *J. Geophys. Res.*, **100**, 18,707–18,726.

A. Albert, V. Echevin, and M. Lévy, Laboratoire d'Océanographie et du Climat: Expérimentation et Analyses Numériques, CNRS/IRD/UPM/MNHN, F-75252 Paris, France. (aurelie.albert@locean-ipsl.upmc.fr)
 O. Aumont, Laboratoire de Physique des Océans, CNRS/IFREMER/UBO, F-29280 Brest, France.